Thermophysics and Aeromechanics, *2018*, *Vol. 25*, *No. 6*

DOI: 10.1134/S0869864318060069

Thermoviscous fluid flow modes in a plane nonisothermal layer*

Y.M. Kulikov and E.E. Son

Joint Institute for High Temperatures RAS, *Moscow*, *Russia*

E-mail: kulikov-yurii@yandex.ru; son.eduard@gmail.com

(*Received June 13*, *2018*; *in revised form August 27*, *2018*)

This paper deals with 3D flow of thermoviscous fluid in the low compressibility approximation within a cubic-shaped domain enclosed between two flat plates with different temperatures. For two other directions, the problem statement assigns periodic boundary conditions, while the steady pressure drop is sustained for the head flow direction. Such formulation allows to trace the evolution of initial disturbances imposed on the main flow depending on perturbation properties. In this case, we consider a degenerate one-dimensional divergence-free noise that is modified by a special correlation filter. When the divergent noise is generated, the solenoid nature of random velocity field must be restored. The simulation demonstrates that random disturbance field development leads to two different scenarios: for the first low-amplitude case, the velocity profile loses initial inflection point and its flowrate increases by 1.5–1.6 times, but for the second one, the flow turbulization occurs destroying the flow core and decreasing the flowrate. In both outcomes, the transition to a steady flow mode in terms of either stationary velocity fields or statistical averages takes place for a long interval: up to $t \sim 200$ dimensionless time units. The analysis of simulated flow is based on integral kinetic energy curves and enstrophy and also via spatial averaging of the obtained data arrays.

Keywords: thermoviscosity, inflection point, random noise, mixing, correlation filter, correction for divergence, turbulence.

Introduction

Study of turbulence remains an important issue due to both fundamental significance of this phenomenon being the only unresolved problem of classical physics [1] and daily practice of mechanical engineering. A multitude of features inherent in turbulence, such as non-organized chaotic (apparently random) behavior, a wide range of time and spatial scales, complex vorticity field and intermittency arise due to interaction of dissipative and nonlinear terms of Navier–Stokes equations which are the basis for describing this phenomenon. Moving beyond bare listing of its typical features, one can quote one of the most up-to-date definitions of turbulence [1], that in mathematical sense is any chaotic solution of 3D Navier–Stokes equations being sensitive to initial data and which is produced in a sequence of instabilities of laminar flow as the bifurcation parameter takes sequentially the values from an increasing sequence. This definition, in our opinion, is a development of the considerations given in [2] and implicitly

* Research was performed due to State Scientific Program of JICT on direction No.15 "Study of electrophysical and thermal processes in multiphase and reacting media", Project 01201357834.

suggests that turbulence properties are determined by the conditions of its origin, in particular, by the initial disturbances and laminar-turbulent transition.

The flow simulation was performed using an in-house implementation of CABARET scheme in the weak-compressibility approximation. This approach derived in [3, 4] has recently been used for solving various problems in different fields of CFD, such as gas dynamics [5], acoustics [6], chemically reacting flows [7], incompressible fluids [8]. The papers [9–14] presented results of thermoviscous fluid (TVF) flow investigations demonstrating its unusual properties in nonuniform temperature fields.

The present research extends the experience of using low compressibility approximation when modeling free shear or channel flows. In particular, in article [15], it was shown that TVF flow velocity profile can contain an inflection point whose location for a given fluid is determined only by the temperature difference ΔT across the channel, which is part of the dimensionless parameter α, while the entrance length appears to be an abrupt function of α. Additionally, the variation of this parameter has the strongest effect on the neutral stability curves, shifting them to the region of small Reynolds numbers Re and long-wave perturbations [16].

The paper [17] describes the modeling of flow mixing in a plane channel caused by harmonic disturbances. A simulation of free shear layer [18] qualitatively confirmed the main results of experimental study [19]. The features of three-dimensional implementation of the scheme used in this paper have been discussed in the simulation of Taylor–Green problem [20].

Various tests of CABARET numerical scheme with low compressibility approximation employed [21] show that flow transition to a particular state takes a lot of computational time especially in the case of 3D problem. Thus, such a problem formulation appears to be inappropriate for mass calculations. To overcome this obstacle one can assign analytically derived velocity profile of TVF flow for a given pressure drop. In 2D computations [17] performed, the wall-normal disturbances were transferred from the inlet boundary by the main flow and produced "destruction" of the flow at the distance of 20 scale units. Actually, this approach includes solving flow stabilization problem containing regular spatial structures.

This paper presents the general problem formulation concerned with initial velocity field assignment and its subsequent modification by solenoidal and correlation filters. The statement of periodic boundary conditions in a plane layer with assigned pressure gradient is explained. The paper also presents brief comments about program implementation and provides the analysis of spatial averaging of several flow modes.

1. Problem statement

1.1. Velocity distribution in the main flow and temperature fields

Computation of thermoviscous flow possessing an abrupt viscosity dependence on temperature T given by formula

$$\mu = \mu_0 e^{\beta(T-T_0)/T_0}, \tag{1}$$

(where μ_0 and T_0 are the reference values for viscosity and temperature) is performed for a cubic-shaped domain with the dimensions $L_X = L_Y = L_Z = L$, being periodically extended in directions X and Y and also restricted in direction Z by walls with different temperature: T_0 — at the lower wall and $T_0 + \Delta T$ — at the upper one complemented by no-slip conditions for fluid particles. The velocity profile for the main flow is set in the form [15]:

$$U_{\text{prof}}(Z) = -\frac{Ce^{-\alpha z/L}}{\alpha(e^{\alpha}-1)}\left(L - Le^{\alpha z/L} - Z + Ze^{\alpha}\right), \quad Z \in [0, L], \tag{2}$$

where $\alpha = \beta \Delta T / T_0$ is a dimensionless parameter,

$$C = (L^2 / \mu_0) \cdot (\Delta p / L) \tag{3}$$

simultaneously with the pressure drop Δp sustained in streamwise direction X and initial temperature distribution

$$T(Z) = (\Delta T / L) Z + T_0. \tag{4}$$

The dimensionless α is chosen so that the profile inflection point and high-speed flow core are far enough from the walls (Fig. 1). Static pressure and density are related through the low compressibility approximation:

$$p = c^2 (\rho - \rho_0), \tag{5}$$

where c, ρ, and ρ_0 stand for sound speed, local and reference densities, correspondingly. The speed of sound c is to ensure the value of Mach number M for the whole computation domain satisfying the inequality

$$\mathrm{M}^2 = \left(\max \left[U, V, W \right] / c \right)^2 \le 0.01. \tag{6}$$

For the case of free shear flows, the dimensionless time variable t can be calculated from the typical velocity U_0 and the initial momentum thickness $\delta_{\theta,0}$ by ratio $t = \tilde{t}\, U_0 / \delta_{\theta,0}$, where $\tilde{t}$ is the physical time [13]. In the present study, we use the channel length L (domain extent in X direction) instead of momentum thickness. Beside the typical time value $t_0 = L / U_0$, we introduce a set of Reynolds numbers Re:

$\mathrm{Re}_1 = U_0 L \rho_0 / \mu_{\mathrm{mean}}$, with U_0 as the initial mass-averaged streamwise velocity, L as the channel height, ρ_0 as the reference density, and μ_{mean} as the mass-averaged viscosity;

$\mathrm{Re}_2 = U^* L \rho_0 / \mu_{\mathrm{mean}}$, where $U^* = U(Z)$ is the local velocity of the main flow; see the description of other parameters as above;

$\mathrm{Re}_3 = U^* L \rho_0 / \mu^*$, where $\mu^* = \mu(Z)$ is the local dynamic viscosity (a function of channel width); see the description of other parameters as above;

$\mathrm{Re}_4 = U_0 L \rho_0 / \mu^*$, see the description of other parameters as above;

$\mathrm{Re}_5 = U^* z^* \rho_0 / \mu_{\mathrm{mean}}$, where z^* is the distance to wall, notably this number is defined for the area $|z^*| \le 0.15 \cup |L - z^*| \le 0.15$; see the description of other parameters above.

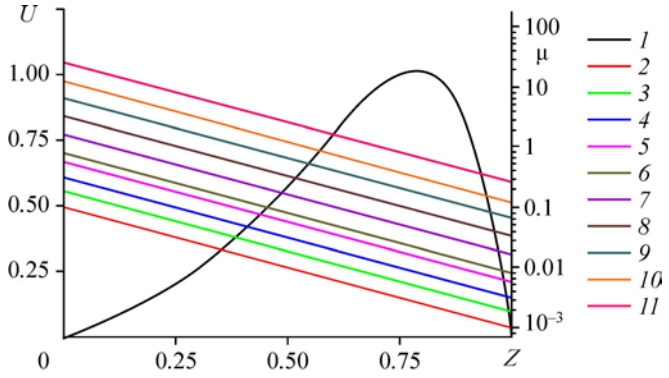

Fig. 1. Distribution of velocity profile ($U = U(Z)$) and dynamic viscosity ($\mu = \mu(Z)$) at different values of μ_0.

1 — $U(Z)$, μ_0 = 0.1 (*2*), 0.2 (*3*), 0.4 (*4*), 0.6 (*5*), 0.8 (*6*), 1.6 (*7*), 3.2 (8), 6.4 (*9*), 12.8 (*10*), 26.6 (*11*), superficial number Re_1 = 4704 (*2*), 2353 (*3*), 1177 (*4*), 788 (*5*), 588 (*6*), 294 (*7*), 197 (*8*), 92 (*9*), 36 (*10*), 18 (*11*).

This variety of Re numbers introduced is caused by a drastic change of velocity profile and dynamic viscosity in wall-normal direction. Obviously, the parameters based on mass-averaged values may be misleading when they are used to describe fluid behavior within different layers especially at the stage of instability development. In fact, a strong variation of viscosity across the channel provides the possibility for different flow modes to exist simultaneously in the sublayers with different temperatures, partly because different viscous shear stresses are important at shear instability growth stage. Figure 2 demonstrates the typical profiles for local Reynolds numbers $\mathrm{Re}_{2,3,4,5} = \mathrm{Re}_{2,3,4,5}(Z)$ for the case of mass-averaged $\mathrm{Re}_1 \approx 588$. These curves pose a serious challenge when interpreting flow properties in terms of dimensionless parameters, as, firstly, it is difficult to outline a priori if one of the listed parameters can be a criterion that determines future evolution of the flow. Secondly, no one can deduce which of presented numbers $\mathrm{Re}_1 - \mathrm{Re}_5$ is the best option for describing the flow pattern. We should note here that in numerous theoretical studies, the Reynolds number is used for estimating the spatial and temporal scales of the vortex flows, mesh resolution quality, and total computational cost $C(\mathrm{Re}_1)$. For the case of uniform isotropic turbulence, the relation of typical scales and oscillation frequencies in the inertia interval yields the following evaluation:

$$C(\mathrm{Re}_1) \sim \mathrm{Re}_1^{11/4}. \tag{7}$$

There is more stringent condition supposing that the time step is related to Kolmogorov scale by the Courant ratio for explicit numerical schemes, that is

$$C(\mathrm{Re}_1) \sim \mathrm{Re}_1^{3}. \tag{8}$$

On one hand, the actual value of mass-averaged Re_1 reckons the flow to the stable laminar mode, but on the other hand, the maximal values of $\mathrm{Re}_2 \approx 1200$ in the flow core testify about possibility for disturbance growth and development of periodic motions.

Re_3 number being defined from local viscosity and velocity demonstrates massively more higher values, which starting from $Z \geq 0.5$ belong to laminar-turbulent transition range ($\mathrm{Re}_1 \approx 2300$ for a pipe flow). Indeed, in the vicinity of Reynolds maximum occurring closer to the hotter wall at $Z \approx 0.9$, Re_3 belongs to mixing transition range ($\mathrm{Re}_1 \approx 10000$, see [22]).

Re_4 number defined by the variable viscosity monotonically increases towards the hot wall and its values remarkably assume the possibility of turbulent transition for the range $0.5 \lesssim Z \lesssim 0.6$. Using this type of dimensionless number allows to distinguish two layers within the flow: the first one is a stable laminar layer, while the second one becomes turbulent.

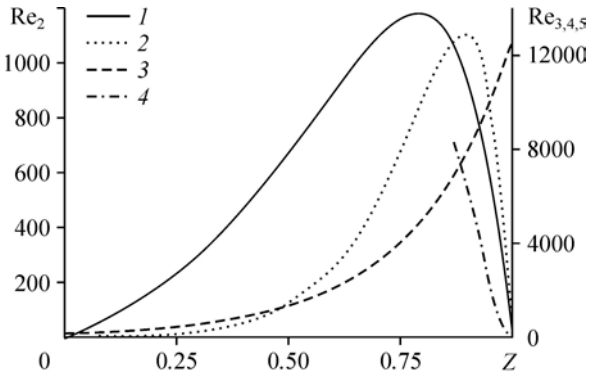

Fig. 2. Spatial distribution of Reynolds numbers Re_2 (*1*), Re_3 (*2*), Re_4 (*3*), Re_5 (*4*) at the mass-averaged $\mathrm{Re}_1 = 588$.

However, the over-estimate of Reynolds Re_4 in the hot near-wall region casts doubts on its consistence.

The near-wall Reynolds number Re_5 is needed for describing turbulence in the boundary layer and in the definition area is comparable to $\mathrm{Re}_{3,4}$, that on formal level means the possibility of a developed turbulent flow in the near-wall layer.

1.2. Assigning the noise with proper correlation characteristics

Modeling consistency of any physical phenomenon is ensured not only by the properties of the numerical method but also by a correct setting of the initial and boundary conditions. When simulating turbulence any researcher encounters a "circulus vitiosus" [23], as to obtain adequate results it is necessary to set main turbulence characteristics in advance. There are several numerical approaches which resolve the above issue, such as setting periodic boundary conditions, downstream velocity field rescaling [24] at the inlet boundary (obtaining instant patterns of random velocity fields), utilizing Karman's energy spectrum in the Fourier space, and also preliminary auxiliary simulations. The latter approach was used in turbulent transition studies when the initial and boundary conditions were taken from properties of the most unstable modes of Orr–Sommerfeld equation [25].

The simplest method for assigning turbulent flow is to superimpose random fluctuations and the average velocity profile. Since the random quantity energy spectrum obtained by computer pseudo-random generators has a uniform distribution for the entire range of wavenumbers (considering the spectral approach). Therefore, the lack of energy in the long wavelength interval results either in a delay of the flow turbulization or faster decay of turbulence, i.e., flow laminarization [23]. This fact was confirmed in test simulations carried out by the authors, but it is not in a focus of the present study.

In general, assigning Gaussian distribution for the autocorrelation function is enough to simulate the pattern of isotropic turbulence. Moreover, one can generate artificial initial data with pre-determined statistic properties obtained experimentally, such as mean values, autocorrelation and cross-correlation functions as well as high-order moment coefficients.

The general algorithm of modified random noise has several steps: (1) — finding the processor seed length, (2) — seed sequence modification, (3) — generation of a new random distribution for the interval [−1, 1] that can be processed by other filters. Here we describe a digital filter [23] for a random field used for assigning an initial set of data and defining a two-point correlation based on the random sequence x'_m, such that $\overline{x'_m} = 0$, $\overline{x'_m x'_m} = 1$, herein the overline means the averaging for the members of sequence. The following convolution defines a digital linear non-recursive filter:

$$x''_m = \sum_{n=-W_f^X}^{W_f^X} b_n x'_{m+n}, \tag{9}$$

where b_n are filter coefficients, W_f^X is the support of the filter. Since we have $\overline{x'_m x'_n} = 0$ at $m \neq n$, the expression

$$\frac{\overline{x''_m x''_{m+k}}}{\overline{x''_m x''_m}} = \sum_{j=-W_f^X+k}^{W_f^X} b_j b_{j-k} \Big/ \sum_{j=-W_f^X}^{W_f^X} b_j^2 \tag{10}$$

is a relation between the filter coefficients and autocorrelation function for x''_m. The filtration can be generalized for the case of three-dimensional random field; this is a convolution for three one-dimensional filters:

$$b_{ijk} = R_S b_X(i) b_Y(j) b_Z(k), \tag{11}$$

where R_S is an additional parameter changing the amplitude at filtration. To invert the expression (10) we have to know the autocorrelation function $R_{x''x''}(\vec{x}, \vec{r})$ (where $\vec{x}$ is a radius-vector of initial point) and/or use the concept of correlation length. The assumption of uniform turbulence means that the correlation function depends on the distance between the points $r = |\vec{r}|$, then the correlation function takes the form:

$$R_{x''x''}(r, 0, 0) = \exp\left(-\pi r^2 \Big/ 4\left(l_c^X\right)^2 \right),\ R_{x''x''}(0) = 1,\ \lim_{r\to\infty} R_{x''x''}(r) = 0. \tag{12}$$

Taking the mesh set with the spatial step Δx and correlation length $l_c^X = n_c^X \Delta x$, we obtain the following:

$$\frac{\overline{x''_m x''_{m+k}}}{\overline{x''_m x''_m}} = R_{x''x''}(k\Delta x) = \exp\left(-\frac{\pi (k\Delta x)^2}{4(n_c^X \Delta x)^2} \right) = \exp\left(\frac{\pi k^2}{4\left(n_c^X\right)^2} \right), \tag{13}$$

and filtration coefficients take the form:

$$b_k \approx \frac{\tilde{b}_{\tilde{k}}}{\sum_{j=-W_f^X}^{W_f^X} \tilde{b}_j^2},\ \tilde{b}_k = \exp\left(-\frac{\pi k^2}{2\left(n_c^X\right)^2} \right). \tag{14}$$

The accuracy of approximation (13) is found from the relation:

$$\max_k \left| \exp\left(-\frac{\pi k^2}{4\left(n_c^X\right)^2} \right) - \sum_{j=-W_c^X+k}^{W_c^X} b_j b_{j-k} \Big/ \sum_{j=-W_c^X}^{W_c^X} b_j^2 \right| \le 0.001 \tag{15}$$

for $W_f^X \ge 2n_c^X$, n_c^X = 2–100. The inequality (15) dictates that the filter support must be higher than the correlation length doubled. The filtration procedure requires the assigned correlation lengths for the corresponding spatial directions $l_c^X = n_c^X \Delta x$, $l_c^Y \Delta y$, $l_c^Z = n_c^Z \Delta z$ and the digital filter support W_f^X, W_f^Y, W_f^Z. The velocity field after filtration is found from the following convolution:

$$v'(i, j, k) = \sum_{i=n_X}^{n_X} \sum_{j=n_Y}^{n_Y} \sum_{k=n_Z}^{n_Z} b_X(i') b_Y(j') b_Z(k') A(i+i', j+j', k+k'), \tag{16}$$

wherein A is an initial random array.

The resulting field of turbulent fluctuations might have the divergence different from zero. At least, the authors of the method did not claim this [23]. Figures 3*a* and 3*b* show an example of velocity autocorrelation curves $R_{UU}(r/L)$ and $R_{VV}(r/L)$ for directions X and Y plotted versus dimensionless distance between the correlation points r/L. Since the convolution of the random velocity field and filter coefficients lack any assumption about periodicity in the computation domain, this means a smaller amount of points for the sample with r increase. Thus, at $r/L > 0.5$ such amount of points is insufficient for calculating reliable values. Nevertheless, we observe a decline in correlation functions (even small negative values for the interval 0.1–0.2) being in compliance with the characteristic correlation length assigned by the filter ($L/8$, see Tables 1 and 2).

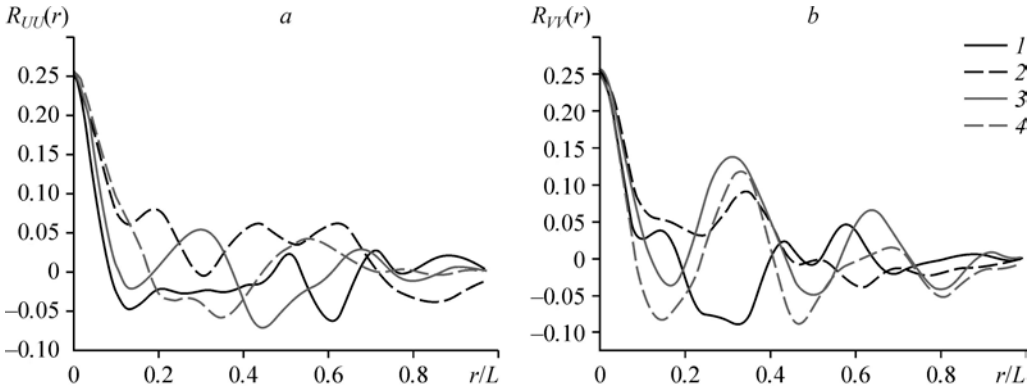

Fig. 3. Autocorrelation functions $R_{UU} = R_{UU}(r/L)$ (*a*) and $R_{VV} = R_{VV}(r/L)$ (*b*) in directions *X* and *Y*, correspondently, at Reynolds numbers $Re_1 = 588$ (*1*, *2*), 788 (*3*, *4*). Computations at meshes 64^3 and 128^3. Mesh sizes 64^3 (*1*, *3*), 128^3 (*2*, *4*).

1.3. Solenoidal filtering

In the problem under consideration, fluid compressibility can be a significant factor for the main flow. Generated turbulence creates the zones of strong vorticity and pressure gradients comparable with gradients for the main flow. Therefore, there is a need to minimize the influence of initial fluctuation field divergence with account for spatial periodicity in directions *X* and *Y*. Spectral methods allow to assign solenoidal field in the simplest way via the scalar product of the wave vector $\vec{k}$ and Fourier-component of velocity $\overrightarrow{u'_k}$ [26]:

$$\left(\vec{k},\ \overrightarrow{u'}_k\right) = 0. \tag{17}$$

The same result can be achieved by generating random functions *f* and *g*, and then, applying the rules of vector algebra, set solenoidal 3D field $\nabla f \times \nabla g$ [27]. Using iterative methods for creating solenoidal velocity field [28] is another option.

For the goals of present paper we implemented the algorithm of divergence correction [29] in formulation [30] that reconstructs the solenoidal field through minimization of the distance to the initial data using the least squares technique provided mass conservation. This yields the following system of equations:

Table 1

List of main parameters for computations

Parameters	Symbol	Value
Reference temperature	T_0	127
Temperature at bottom wall	T_1	127
Temperature at top wall	T_2	273
Exponent index	β	–4
Dimension of simulation domain	L	0.2
Reference density	ρ_0	1000
Thermal conductivity	λ	0.3
Heat capacity	C_p	2000
Courant number	CFL	0.15

Table 2

Additional parameters

Calc. number	Reference viscosity, μ_0	Pressure drop, Δp	Bulk mean Reynolds number, Re_2	Numerical grid, $n_X \times n_Y \times n_Z$	Typical correlation lengths, (n_c^X, n_c^Y, n_c^Z)	Half-width of filter, (W_f^X, W_f^Y, W_f^Z)	Amplitude parameters, Re_3	Turbulence intensity, $l_X \times 10^{-2}$	Turbulence intensity, $l_r \times 10^{-2}$
1	26.6	81.92	18	64^2	(4, 4, 4)	(12, 12, 12)	1.0	2.1	2.1
2	12.8	40.96	36					2.1	2.8
3	6.4	20.48	92					1.7	1.9
4	3.2	10.24	197					1.8	3.4
5	1.6	5.12	294				1.25	2.4	1.7
6a	0.8	2.56	588	64^2				1.8	2.4
6b				128^2	(8, 8, 8)	(24, 24, 24)	5.0	3.6	4.4
7a	0.6	1.92	788	64^2	(4, 4, 4)	(12, 12, 12)	1.0	2.5	3.1
7b				128^2	(8, 8, 8)	(24, 24, 24)	4.0	2.7	2.4
8a	0.4	1.28	1177	64^2	(4, 4, 4)	(12, 12, 12)	1.25	3.0	2.7
8b				128^2	(8, 8, 8)	(24, 24, 24)	5	2.4	3.5
8c				128^2			8	1.5	1.1
10a	0.2	0.64	2353	64^2	(4, 4, 4)	(12, 12, 12)	0.5	2.9	2.7
10b				128^2	(8, 8, 8)	(24, 24, 24)	5	4.6	5.3
11a	0.1	0.32	4707	64^2	(4, 4, 4)	(12, 12, 12)	1.25	2.7	2.5
11b				64^2				5.3	4.6
11c				64^2				2.1	2.2
11d				128^2	(12, 12, 12)	(24, 24, 24)	5	4.1	4.1

$$\begin{cases} \min \sum_{i,\,j,\,k=1}^{n_X,\,n_Y,\,n_Z} \left(u_{\text{init}}^{ijk} - u_{\text{corr}}^{ijk}\right)^2 + \left(v_{\text{init}}^{ijk} - v_{\text{corr}}^{ijk}\right)^2 + \left(w_{\text{init}}^{ijk} - w_{\text{corr}}^{ijk}\right)^2, \\ \sum_{i'=1}^{nX} d_{n_X}^{ii'} u_{\text{corr}}^{i'jk} + \sum_{j'=1}^{n_Y} d_{n_Y}^{jj'} u_{\text{corr}}^{ij'k} + \sum_{k'=1}^{n_Y} d_{n_Z}^{kk'} u_{\text{corr}}^{ijk'} = 0, \end{cases} \tag{18}$$

where u_{init}^{ijk}, v_{init}^{ijk}, w_{init}^{ijk} and u_{corr}^{ijk}, v_{corr}^{ijk}, and w_{corr}^{ijk} are the initial and corrected components of velocity vector, $d_{n_X}^{ii'}$, $d_{n_Y}^{jj'}$, and $d_{n_Z}^{kk'}$ are the one-dimensional discrete mesh differential operators in directions *X*, *Y*, *Z* defined by the difference scheme. For the case of central-difference approximations and accounting for the no-slip boundary conditions, the 1D mesh differential operator takes the form:

$$\begin{pmatrix} -1 & 1 & 0 & \ldots & 0 \\ -1/2 & 0 & 1/2 & \ldots & \ldots \\ \ldots & -1/2 & 0 & 1/2 & \ldots \\ \ldots & \ldots & -1/2 & 0 & 1/2 \\ \ldots & \ldots & \ldots & -1 & 1 \end{pmatrix}, \tag{19}$$

meanwhile for the periodic boundary conditions, the first and last matrix lines are modified, since for this situation, the method takes the values from the opposite boundary:

$$\begin{pmatrix} 0 & 1/2 & 0 & \ldots & -1/2 \\ -1/2 & 0 & 1/2 & \ldots & \ldots \\ \ldots & -1/2 & 0 & 1/2 & \ldots \\ \ldots & \ldots & -1/2 & 0 & 1/2 \\ 1/2 & \ldots & \ldots & -1/2 & 0 \end{pmatrix}. \tag{20}$$

In the case of non-periodic boundary conditions, the matrix is three-diagonal.

There is also a variation of this method utilizing weight coefficients [30]. The optimization algorithm includes several steps.

1. The solution of eigenvalue problem for matrixes $d_{n_X} d_{n_X}^{\mathrm{T}}$, $d_{n_Y} d_{n_Y}^{\mathrm{T}}$, and $d_{n_Z} d_{n_Z}^{\mathrm{T}}$. Eigenfunction decomposition is formulated as

$$\begin{aligned} d_{n_X} d_{n_X}^{\mathrm{T}} &= \Phi_{n_X} \Lambda_{n_Y} \Phi_{n_X}^{\mathrm{T}}, \\ d_{n_Y} d_{n_Y}^{\mathrm{T}} &= \Phi_{n_Y} \Lambda_{n_Y} \Phi_{n_Y}^{\mathrm{T}}, \\ d_{n_Z} d_{n_Z}^{\mathrm{T}} &= \Phi_{n_Z} \Lambda_{n_Z} \Phi_{n_Z}^{\mathrm{T}}, \end{aligned} \tag{21}$$

where Φ_{n_X}, Φ_{n_Y}, and Φ_{n_Z} are the matrices of the left eigenvectors.

2. Calculation of divergence residual

$$S_{init}^{ijk} = \sum_{i'=1}^{n_X} d_{n_X}^{ii'} u^{i'jk} + \sum_{j'}^{n_Y} d_{n_Y}^{n_Y} u^{ij'k} + \sum_{k'}^{n_Y} d_{n_Z}^{kk'} u^{ijk'}, \tag{22}$$

$$\Gamma^{ijk} = \Lambda_{n_X}^{i} + \Lambda_{n_Y}^{j} + \Lambda_{n_Z}^{k}. \tag{23}$$

3. Calculation of Lagrangean multipliers

$$\mu^{ijk} = \sum_{l,m,n=1}^{n_X,n_Y,n_Z} \Phi_{n_X}^{il} \Phi_{n_Y}^{jm} \Phi_{n_Z}^{kn} \Big/ \Gamma_{lmn} \sum_{i',j',k'=1}^{n_X,n_Y,n_Z} \Phi_{n_X}^{i'l} \Phi_{n_Y}^{j'm} \Phi_{n_Z}^{k'n} S_{\text{init}}^{i'j'k'}. \tag{24}$$

4. Updating velocity values

$$u_{\text{corr}}^{ijk} = u_{\text{init}}^{ijk} - \sum_{i'=1}^{n_X} d_{n_X}^{i'i} \mu^{i'jk},$$
$$v_{\text{corr}}^{ijk} = v_{\text{init}}^{ijk} - \sum_{j'}^{n_Y} d_{n_X}^{j'j} \mu^{ij'k}, \tag{25}$$
$$w = w_{\text{init}}^{ijk} - \sum_{i'=1}^{n_X} d_{n_X}^{k'k} \mu^{ijk'}.$$

In this paper, we used the two-dimensional degenerate noise produced by velocity fluctuations in directions of periodicity. So, the initial conditions satisfy a more strict clause than the usual solenoidal field

$$\frac{\partial u'(0)}{\partial x} + \frac{\partial v'(0)}{\partial y} = 0, \tag{26}$$

that is

$$\frac{\partial u'(0)}{\partial x} = 0, \ \frac{\partial v'(0)}{\partial y} = 0, \tag{27}$$

and we assume in advance that $u'(0, y) = u'(y)$ and $v'(0, x) = v'(x)$. This simplification, in particular, allows avoiding to adopt the described filter for divergence correction in 3D case overloaded by nine imbedded loops at the step of Lagrangean multipliers calculation. However, for 2D divergent noise, this algorithm appears to be efficient and fast. Obviously, the characteristics of generated two-dimensional noise are not quite adequate for describing real three-dimensional field of chaotic fluctuations. Therefore, the noise generated can be used in modeling under assumption that 3D turbulence has rather short history. Conversely, it affords to trace the energy transfer to initially zero component of velocity between two plates.

2. Boundary conditions for CABARET numerical method

CABARET scheme in its initial formulation contains the equations written both in conservative and characteristic forms leading to a superset of meshes for so-called conservative and flux variables. The latter can include few more sets according to the number of transfer directions for local Riemann invariants. These ensembles are distributed in different manner within the domain: the conservative variables points are located at the centers of computational cells (and enumerated by integers), while the flux variable points are placed in the middles of cell faces and indexed by fractional numbers. The monograph [31] presents the most general collection of CABARET variations, and the current implementation for 2D domain was discussed in [21].

In problem presented here, we set small-scale turbulent fluctuations on the steady velocity profile as the initial condition and observe their evolution in time in a periodic channel. We also assume that the mesh has (n_X, n_Y, n_Z) cells in corresponding spatial coordinates. To keep a steady pressure drop Δp and velocity transfer all the local Riemann invariants determining boundary conditions have discontinuity at the boundary.

Using the Riemann invariants for low-compressible fluid being responsible for the transfer of disturbances one can write:

— along X-direction

$$I_1^X = c\ln(p + c^2\rho_0) + u, \quad \lambda_1^X = u + c,$$
$$I_2^X = -c\ln(p + c^2\rho_0) + u, \quad \lambda_2^X = u - c, \tag{28}$$
$$I_3^X = v, \ I_4^X = w, \ I_5^X = w, \ \lambda_{3,4,5}^X = u,$$

— along *Y*-direction

$$
\begin{aligned}
&I_1^Y = c\ln(p + c^2\rho_0) + v, \quad \lambda_1^Y = v + c,\\
&I_2^Y = -c\ln(p + c^2\rho_0) + v, \quad \lambda_2^Y = v - c,\\
&I_3^Y = u,\ I_4^Y = w,\ I_5^Y = T,\ \lambda_{3,4,5}^Y = v,
\end{aligned}
\tag{29}
$$

— along *Z*-direction

$$
\begin{aligned}
&I_1^Z = c\ln(p + c^2\rho_0) + w, \quad \lambda_1^Z = w + c,\\
&I_2^Z = -c\ln(p + c^2\rho_0) + w, \lambda_2^Z = w - c,\\
&I_3^Z = u,\ I_4^Z = v,\ I_5^Z = T,\ \lambda_{3,4,5}^Z = w.
\end{aligned}
\tag{30}
$$

Let us construct the boundary conditions for the computational domain shown in Fig. 4.

2.1. *Periodic boundary condition retaining the pressure drop*

When calculating flux variables in the boundary cells, we have to introduce two additional layers wherein flux variables (ρ, u, v, w) are transferred from the opposite boundary, furthermore, the density values must be corrected accounting for the pressure drop Δp between the boundaries.

Therefore, the layer at the inlet left boundary receives the variables $(\rho(i, j, n_X) + \Delta p / c^2$, $u(i, j, n_X)$, $v(i, j, n_X)$, $w(i, j, n_X)$, $T(i, j, n_X))$ subsequently providing the value I_1^X spreading downstream. Invariants I_1^X and I_2^X being transferred from the computational domain interior allow finding the flux variables at the inlet boundary. Similarly, there is an additional layer $(\rho(i, j, 1) - \Delta p / c^2$, $u(i, j, 1)$, $v(i, j, 1)$, $w(i, j, 1)$, $T(i, j, 1))$ for the outlet boundary that is used to obtain I_2^X, meanwhile invariant I_1^X contains the information from the internal points. Finally, we get a space-periodic flow with a dummy density discontinuities at the inlet and outlet. This approach allows us avoiding simulating the processes of velocity and temperature field stabilization and spreading of turbulent fluctuations downstream that saves processor time.

From the physical point of view, using such boundary conditions means assigning the spatial turbulent field in the fluid volume that passes many times through the same rectangular-sectioned channel portion.

Nonlinear properties of low-compressible fluid invariants with respect to pressure p causing under certain conditions algorithm malfunction are serious issue at the preliminary stage when tuning parameters (the Courant number, for example) are not well defined. The developed approach poses an unsettled

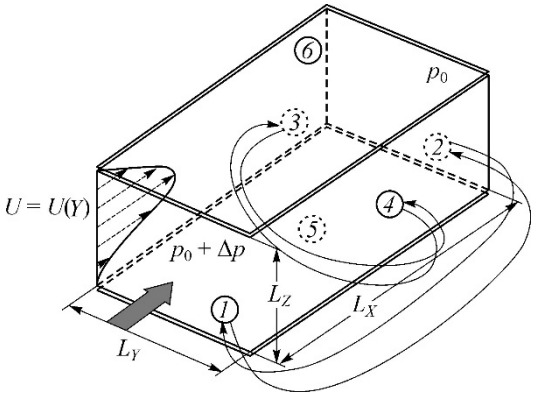

Fig. 4. Computational domain diagram. Boundaries are marked by digits *1*–*6*; the interrelated boundary conditions are shown with double arrows, the solid broad arrow depicts the main flow direction $U = U(Z)$ (boundaries *1*, *2*), dashed arrows show the initial projection of a flat profile on the boundary number *3*.

issue of acoustic disturbances spreading streamwise (effect of "the future" on "the past"). This kind of boundary conditions are available in literature, but not for Riemann invariants.

2.2. *Periodic boundary conditions on the front face (3) and rear face (4) as shown in Fig. 4*

These boundary conditions also require two additional layers (without density discontinuity) on the front face $(\rho(i,n_Y,j),\ u(i,n_Y,j),\ v(i,n_Y,j),\ w(i,n_Y,j),\ T(i,n_Y,j))$ and rear face $(\rho(i,1,j),\ u(i,1,j),\ v(i,1,j),\ w(i,1,j),\ T(i,1,j))$ to compute the invariants I_1^Y and I_2^Y.

2.3. *No-slip conditions for the flux variables in planes 5 and 6 depicted in Fig. 4*

The no-slip conditions on walls 5 and 6 (Fig. 4) are written in a simple way: $(u(i,j,1/2),\ v(i,j,1/2),\ w(i,j,1/2)) = (0,0,0)$ — for the lower wall. The calculation of pressure is performed via the invariant I_2^Z transferring information from the domain interior. On the upper wall, this condition is written as $(u(i,j,n_Z+1/2),\ v(i,j,n_Z+1/2),\ w(i,j,n_Z+1/2)) = (0,0,0)$, and the pressure is defined from I_1^Z, containing the information from the inner cells. The boundary conditions for speeds are supplemented by the condition of constant temperature at the lower $T(i,j,n_Z+1/2) = T_0$ and upper $T(i,j,n_Z+1/2) = T_0 + \Delta T$ walls.

Computations were performed on rectangular grids with a number of cells equal in all directions, — 64^3 and 128^3. As the CABARET scheme belongs to the class of explicit numerical methods, the stability conditions bound transient and spatial steps calculated from the channel size L. This feature increases computational time during mesh refinement across the channel (especially at long time of flow stabilization). Thus, the meshes used allow to simulate essentially large-scale flows. The list of parameters being constant for all tests are presented in Table 1. The initial data changing in test series are summarized in Table 2. The supplementary diagram of initial turbulence intensity is depicted in Fig. 5.

3. Remarks on software implementation

The CABARET algorithm for low-compressible fluid was implemented in Fortran F90 using hybridized parallel technique via OpenMP and MPI. Computations were performed on

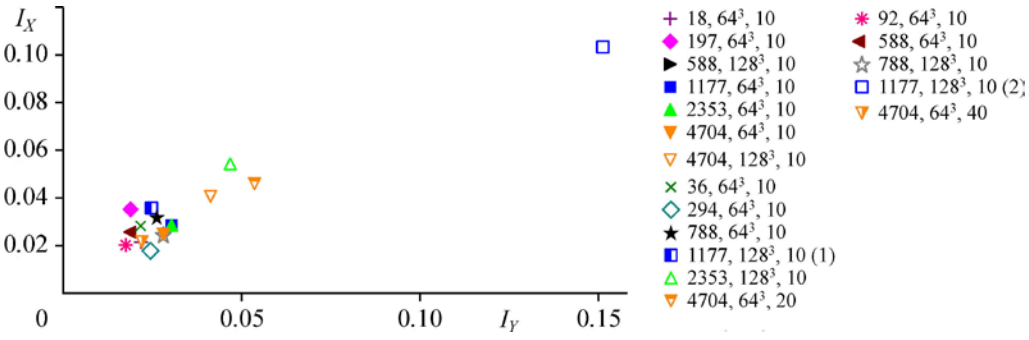

Fig. 5. Diagram for intensity of initial disturbances in directions *X* and *Y*.
The numbers next to symbols correspond (left to right) to Reynolds number Re_1, size of grid, sound velocity; the numbers in parenthesis (1) and (2) indicate the computations (10) and (11) performed for $\mathrm{Re}_1 = 1177$ and different in initial intensity of disturbance.

computers from JIHT RAS and on MVS-10p (JSCC RAS). The isothermal flow simulation details were discussed in [21].

4. Averaging methods and results

Turbulence often develops in nonuniform and multicomponent fluids, thus, including the media with different viscosities.

When considering free shear flows, the typical approach is the spatial averaging along the periodical directions. For the case of pressure-driven flow, the averaging in the gradient direction seems inappropriate as turbulence evolves along the channel length. However, for the chosen domain, the length scale subjected to the pressure gradient exactly equals the extents in other directions, whereas the travel time of a fluid particle is small. Consequently, in this paper, we deal with averaging in directions of periodicity X and Y, using the notation $\langle\ \rangle_S$. The spatial averaging allows to obtain time-instant velocity and temperature profiles presented as a color $Z-t$-chart. Integral kinetic energy

$$E(t)=\frac{1}{\rho_0 U_0^2 V}\iiint\limits_{\Omega}\frac{\rho_0(U^2+V^2+W^2)}{2}\,d\Omega, \tag{31}$$

and the integral enstrophy

$$\zeta(t)=\frac{t_0^2}{\rho_0 V}\int\limits_V\frac{\rho\vec{\omega}^2}{2}dV \tag{32}$$

are among the most important flow characteristics. The dependency of integral kinetic energy on time (Fig. 6) has the following properties. As Reynolds number increases in the range Re_1=18–4704, we observe a drastic change in curves behavior. There is a growth of kinetic energy at low Re_1, whereas at higher numbers, the energy declines due to generation of turbulence. At low Reynolds number, the role of viscous shear stress appears to be significant inducing rapid flow transformation causing corresponding changes in kinetic energy. Moreover, we note a rapid grid convergence (e.g., for the flow with Re_1 = 588 on meshes 64^3 and 128^3). A transitional case takes place in the range $\mathrm{Re}_1 > 588 \cap \mathrm{Re}_1 << 2000$: if mesh is coarse the drastic turbulence generation occurs, while on finer grids low-Reynolds mode restores. Starting from $\mathrm{Re}_1 \approx 2300$, the mesh refinement does not change the simulated flow mode. With a further increase in Reynolds number, we observe transition to a "limiting" mode when the curve shape is almost independent of Re_1. It should be noted that for any value of Re_1, there

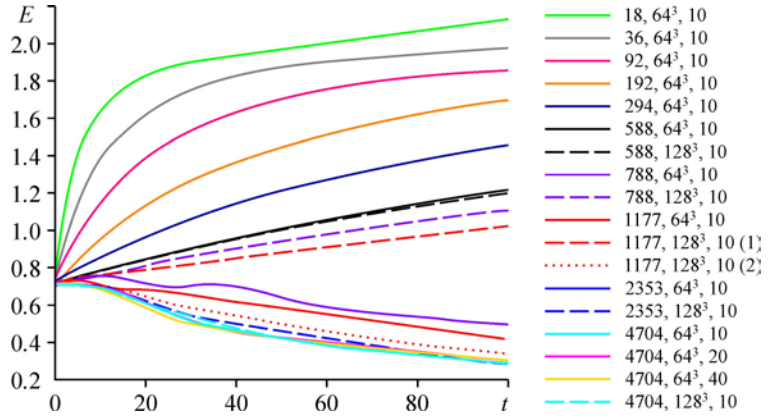

Fig. 6. Dimensionless kinetic energy as function of time (for different Reynolds numbers and for meshes 64^3 and 128^3).
See legend in Fig. 5.

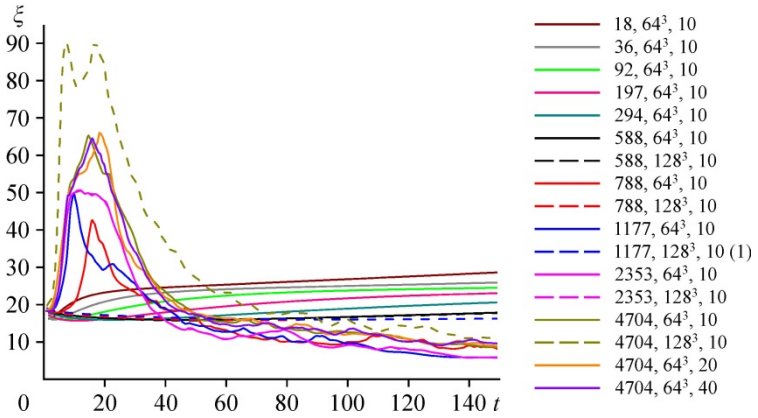

Fig. 7. Dependency of the integral enstrophy on time calculated for different Reynolds numbers on meshes 64^3 and 128^3. See legend in Fig. 5.

is a time t_a, when the kinetic energy takes almost asymptotic value. This transition time possibly marks a new equilibrium state between the flow and corresponding boundary conditions.

Simulations on the coarse grid at $\mathrm{Re}_1 = 4704$ were performed at various sound speeds c and did not show any significant difference between the results.

Integral enstrophy curves pattern (Fig. 7) confirms the co-existence of two regimes for flow evolution: the flow retains the laminar character for one mode, while for another one, we observe a sudden generation of vorticity with energy dissipation. In the latter case, active turbulence generation occurs during the interval $\Delta t \approx 8$–15 depending on Reynolds number. As the Re_1 increases in the range $\mathrm{Re}_1 = 588$–1176, the rate of vortex generation doubles. As for simulations on the coarse mesh, the turbulence decay due to vorticity dissipation occurs in the time scale $t = 20$–150 regardless Reynolds number and sound velocity c. The most rapid (in a time $t \approx 6$) vorticity generation corresponds to the maximal Reynolds number ($\mathrm{Re}_1 = 4704$) simulated on the mesh 128^3.

Let us describe the flow (case $\mathrm{Re}_1 = 588$, 64^3) basing on a set of profiles (Fig. 8), obtained via the averaging in the directions of periodicity. They are plotted as $Z - t$-charts and elucidate the origin of two kinds of dependencies $E = E(t)$. For example, the simulation at low Reynolds number reveals that the temperature field $\langle T \rangle_S$ remains steady for all time-averaged layers, which is not the case for the streamwise velocity $\langle U \rangle_S$ exhibiting flow rearrangement under the influence of small finite-amplitude fluctuations. It is worth noting that there is an increase in flow core velocity and its expansion into the central part of the channel leading to substantional changes of the flowrate. In the problem formulation used the initial velocity profile being matched with the boundary conditions for pressure and thermal characteristics (either inflectional flow profile with a constant pressure drop and no-slip walls with different temperatures T or Poiseuille flow in the absence of speed disturbances) is proven to be unchangeable for infinitely long time interval. The situation changes if the disturbances are imposed: the new flow profile lacks the inflection point and this alters flowrate characteristics. It is important that existence of an inflection point in the velocity profile for a particular fluid is determined only by the temperature drop ΔT. The flow rearrangement occurs due to velocity disturbances which are eliminated after averaging without any growth in the maximal core velocity or core repulsion from the walls. Profile smoothing takes a long time — up to $t \approx 30$. One can assume the loss of algorithm conservation property (rather than the numerical scheme) probably caused by specific boundary conditions applied, but this assumption does not explain inflection point

dying-out and the flowrate stability at the hot near-wall zone. The speculation on decrease in the actual ΔT because of partial mixing in the near-wall zone has not been confirmed. In the reduced form, the flowrate in the streamwise direction $Q(t)/Q(0)$ can be approximated by the function $Q(t)/Q(0) \sim \log(t)$. For the long time evolution, the flowrate curve rests in between two asymptotes $Q(t)/Q(0) \sim b\log(t-a)$ and $Q(t)/Q(0) = 1 + A\exp(-t/t_1)$.

The spanwise velocity component $\langle V \rangle_S$ decays in all layers while the evolution. Thus, for the flow core ($z \approx (0.5–0.75)\,L$) during interval $\Delta t \approx 1.5$ it declines by factor of 3, then almost linear decline occurs with a change of approximately 0.2 from the initial value. In similar way, for the wall-normal cross section, this value retains within core at 0.4–0.8, whilst in the near-wall zone, this quantity decays almost to zero. Thus, the development of 3D flow does not occur. Note here that mesh refinement (for this flow mode) causes the flowrate to change earlier due to the acceleration in the core, that is on mesh 64^3 — at $t \approx 65$, on mesh 128^3 — at $t \approx 39$.

Simulation at moderate Reynolds numbers (Re_1 = 788, 1176) shows (Fig. 9) a turbulent scenario on the coarse mesh, while the fine mesh demonstrates simple flow rearrangement under impact of initial disturbances. For the turbulent scenario, the mixing process can be observed via isolines of temperature $\langle T \rangle_S$. Direct relation of the isoline position and layer ordinate allows to investigate the behavior of certain fluid layers, so one can describe mixing by the isoline shift starting in the upper layer $(0.9–1.0)L$ at $t \approx 9$ and showing after interval $\Delta t \approx 20$ almost complete mixing.

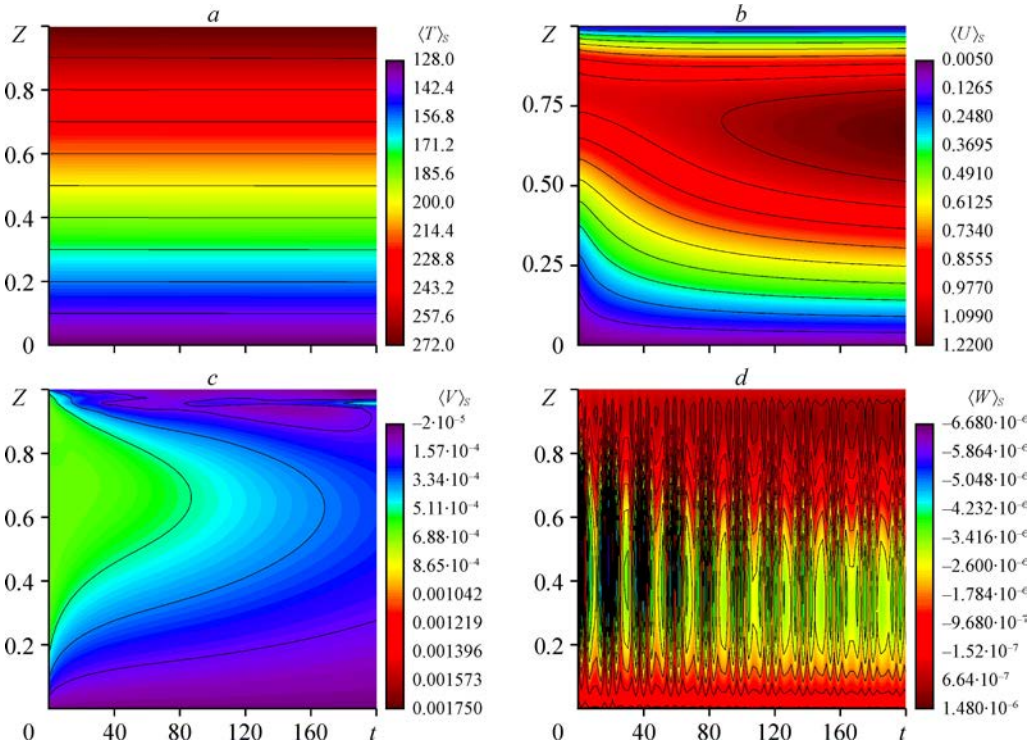

Fig. 8. Z–t-diagrams of temperature $\langle T \rangle_S$ (*a*) and velocity components $\langle U \rangle_S$ (*b*), $\langle V \rangle_S$ (*c*), $\langle W \rangle_S$ (*d*), built from simulation results for $\mathrm{Re}_1 = 588$ on grid 64^3.

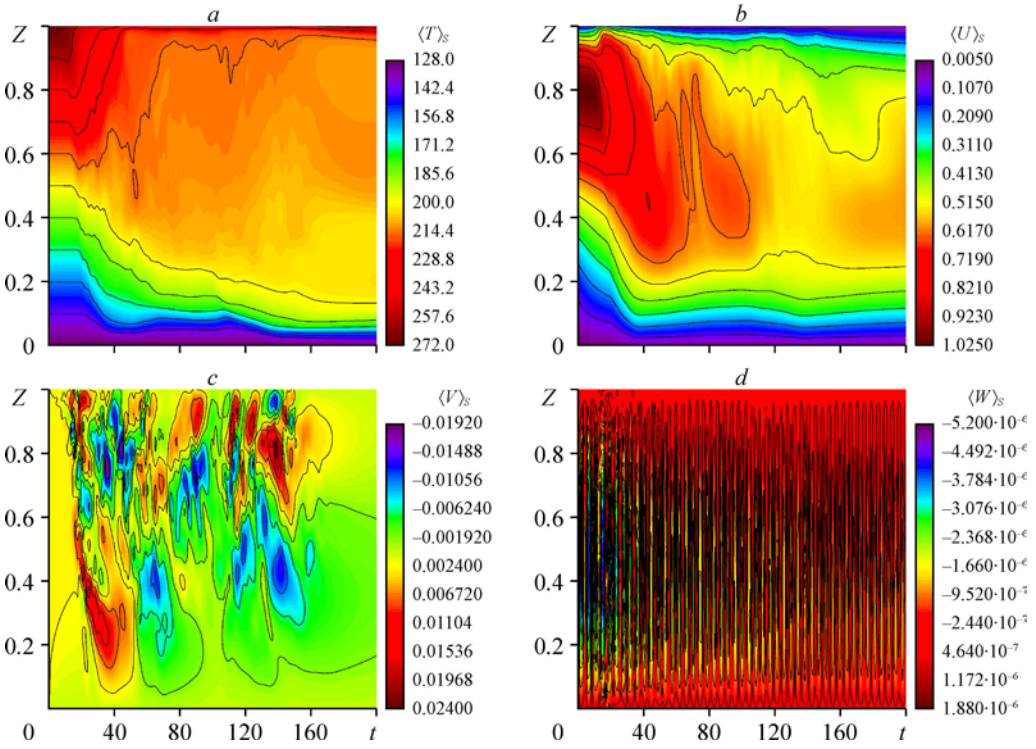

Fig. 9. *Z*–*t*-charts of temperature profiles $\langle T \rangle_S$ (*a*) and velocity components $\langle U \rangle_S$ (*b*), $\langle V \rangle_S$ (*c*), $\langle W \rangle_S$ (*d*) for the case of turbulent flow mode at low Reynolds numbers $\mathrm{Re}_1 = 788$ (for grid 64^3).

As for other layers, the large-scale mixing occurs in the time interval $t \approx 11$–22. Finally, the mixing process causes the expansion of the middle layer $z \in [0.5, 0.6]$, its upper boundary demonstrates a sharp and non-uniform growth in the interval $\Delta t \in 20-60$, while the lower boundary expands smoothly to the cold wall. This broadening has exponential character and occupies a longer time interval $\Delta t \approx 22$–180, and, finally, reaches the position $0.13L$ in the ordinate axis. In the asymptotic state, this layer reaches ordinate 0.95. So by the end of simulation process, the mixing layer (with temperature drop $\Delta T/10$) occupies 0.83 of the entire cross section. As a result, for the long time evolution, the layers $(0.6–1)L$ (in the upper half-plane) transform into a hot sublayer with a small thickness $0.05L$. The layer 0.4–0.5 (see the lower half-plane) remains with the same thickness, but it is fed by cold bottom wall sublayers and drifts in downward direction to the ordinates range 0.085–0.165. As concerns the cold layers, their thickness reduces by 4 times (from 0.4 to 0.085), and finally they occupy a cold near-wall sublayer with the thickness of 0.085 being twice thicker compared to the hot sublayer.

Destruction of the main flow profile occurs at $t \approx 14$. It is accompanied by the large expansion of flow core — from 0.6–0.9 to 0.44–0.9 with corresponding reduction of the maximum. The pattern of average velocity chart is very nonuniform (up to time $t \approx 110$), in further leading to total smearing of central region. At $t > 120$, there is the most active deceleration in the vicinity of the upper (hot) wall, probably caused by fast mixing. The isolines of velocity are shifted to the wall (in the lower half-plane) testifying two-fold shrinking of the layers with corresponding temperature. Additionally, for the upper nearwall zone, the thickness of the upper near-wall layer (velocity range $U \sim (0.3–0.4)U_{\max}$ ($U_{\max} = 1$)) increases in very non-uniform manner (disturbance from large-scale vortices may reach the core and pull it to the bottom wall).

The charts of the velocity component $\langle V \rangle_S$ (in the direction of periodicity) also indicate the existence of a flow mode with preferred velocity direction, in which the two-dimensional flow is realized in terms of average values, although in fact this is three-dimensional flow due to 3D nature of vortices generated.

The graphs of the initially zero velocity field $\langle W \rangle_S$ provide information on the existence of vortices with the vertical component of velocity (that breaks stationary field). It is worth noting that in this case the averaging causes the confusion due to rather large interval between averaged time instants.

The simulation at higher Reynolds number ($\mathrm{Re} = 4704$, grid 128^3, see Fig. 10) shows a more intensive and earlier mixing that can be deduced from corresponding *Z*–*t*-chart for $\langle T \rangle_S$. The time initiation of mixing process is as follows: in the layer 0.0–0.1 — $t \approx 10.68$; in the layer 0.1–0.2 — $t \approx 9.49$; in the layer 0.2–0.3 — $t \approx 7.12$; in the layer 0.3–0.4 — $t \approx 7.12$; in the layer 0.4–0.5 — $t \approx 4.74$; in the layer 0.5–0.6 — $t \approx 4.74$; in the layer 0.6–0.7 — $t \approx 4.74$; in the layer 0.7–0.8 — $t \approx 4.74$; in the layer 0.8–0.9 — $t \approx 2.27$; in the layer 0.9–1 — $t \approx 4.74$. The mixing in the lower half-plane occurs in the time interval $t = 20$–40. The thickness of upper hot sublayer is $0.034L$, while the lower one is $0.023L$, they do not increase in time (in terms of averaged values).

The shape of main flow velocity profile $\langle U \rangle_S$ retains up to $t \approx 4$, and then one can observe deformation in the layer 0.85–1.0 related to acceleration in the nearwall zone and retarding of velocity in the layer closer to the core. Later, a decay of this core and decline of the maximal velocity occur. The profile section $z \in [0, 0, 6]$ with an inflexion point retains up to $t \approx 10$,

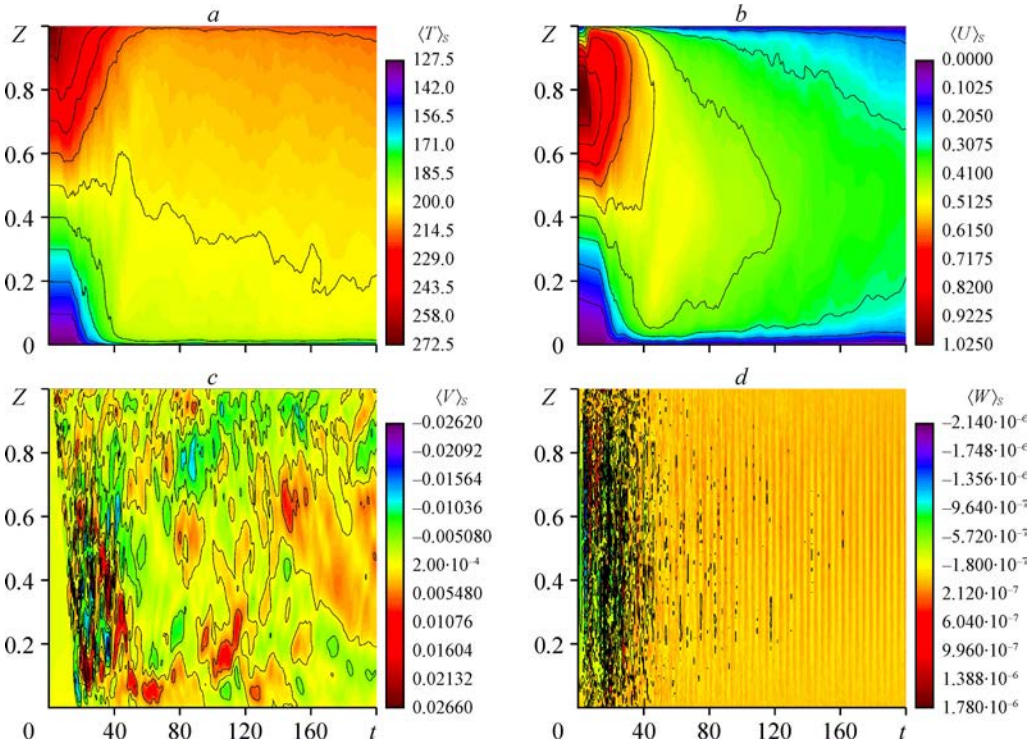

Fig. 10. Z–t-diagrams of temperature profiles $\langle T \rangle_S$ (*a*) and velocity components $\langle V \rangle_S$ (*b*), $\langle V \rangle_S$ (*c*), $\langle W \rangle_S$ (*d*) for the case of turbulent flow mode at Reynolds number $\mathrm{Re}_1 = 4704$ on grid 128^3.

but then it dissipates in the range $t \approx 10–20$. This evolution creates a transitional velocity profile (like an inclined line), which later transforms into Π-shaped turbulent velocity profile.

$\langle V \rangle_S$ -chart demonstrates flow development in spanwise direction: for different layers, the averaged flow is directed in opposite sides. Since we initially assigned the 2D noise, the averaged values probably show the existence of transversal shear layers. The intensity of averaged flow also increases for the interval of mixing and declines by $t \approx 60$, which is interpreted as an indirect support of the layer flow decay and loss of the relation to the initial conditions. Diagram $\langle W \rangle_S$ testifies about existence of strong vortices for the entire cross section of channel, especially for the range $t = 16–50$.

Conclusions

The simulation results of thermoviscous fluid flow in a plane infinite layer (a cubic-shaped domain periodically extended in two directions and limited by two walls with different temperatures) demonstrate the existence of very different flow modes. The first mode corresponds to low (mass-averaged) Reynolds numbers Re_1, and it is related to the rearrangement of unstable inflectional laminar velocity profile forced by 3D disturbances to the stable one, that has higher flowrate properties. In the second mode, turbulence generation occurs with accelerated dissipation of kinetic energy and complex vorticity field.

We should make few comments on the simulation performed in this study. In general case, the successful simulation of a vortex (or turbulent) flow requires an appropriate efficient and low-dispersive (-dissipative) numerical method and consistent turbulent fluctuation properties. To ensure the high resolution of all essential scales one should use finest meshes and then apply the set of digital filters to calculated data for better theoretical analysis. The term “digital filter” is interpreted here in the most general sense; it comprises calculation of integral characteristics, statistical averaging, spectral decomposition (Fourier transformation). In this view, we can indicate some methodological deviations from the above mainstream essentials allowed in the presented paper.

1. Applying specific boundary conditions retaining pressure gradient significantly lowers Courant number required to perform a stable calculation. The increase in CFL makes the expression under logarithms in Riemann invariants to be negative. This negative attribute probably should be referred to the current implementation.

2. The CABARET belongs to the class of explicit methods, therefore, the computational complexity increasing during mesh refinement as N^4, where N is the number of mesh points in one direction, turns into challenging task even for supercomputers.

3. Using different intensities for the same Re_1 at different meshes distorts mathematical rigor. However, this approach allows to evaluate the flow pattern in a wide range of parameters and might only influence the flow before turbulent transition, as the 3D nature of turbulence has relatively short history and «forgets» disturbance properties soon enough. Additionally, the issue if the disturbance intensity and its correlation length are the parameters sufficient to determine uniquely flow evolution in all time intervals (especially during transition to turbulence) remains unsettled. Probably, the flow pattern can be determined by the local amplitude of disturbance. In this case, the generation of random noise on a fine mesh and its sampling for coarse meshes yield different final data sets. In some cases, these sets can contain points of an amplitude exceeding the critical level required for flow rearrangement. In this paper, the noise characteristics are defined from the typical length of correlation (and intensity of noise in directions X and Y), however, the question of other statistical properties of the filtered velocity field,

such as averaged intensity and dispersion obtained from an ensemble of realizations is not in the focus of current study.

4. The correlation filter has many parameters and makes difficult comparative analysis of transitional modes, including the stage of large-scale mixing.

5. The extraordinarily long process of flow stabilization, possibly, was caused by using low compressibility approximation.

References

1. **J.M. McDonough,** Introductory Lectures on Turbulence, CreateSpace Independent Publishing Platform, 2014.
2. **A.S. Monin,** On the nature of turbulence, Physics-Uspekhi, 1978, Vol. 21, No. 5, P. 429–442..
3. **V.M. Goloviznin and A.A. Samarskii,** Finite difference approximation of convective transport equation with space splitting time derivative, Matematicheskoe Modelirovanie, 1998, Vol. 10, No. 1, P. 86–100.
4. **V.M. Goloviznin and A.A. Samarskii,** Features of differential scheme CABARET, Matematicheskoe Modelirovanie, 1998, Vol. 10, No. 1, P. 101–166.
5. **S.A. Karabasov and V.M. Goloviznin,** Compact accurately boundary adjusting high–resolution technique for fluid dynamics, J. Comput. Phys., 2009, Vol. 229, No. 19, P. 7426–7451.
6. **V.M. Goloviznin, S.A. Karabasov, T.K. Kozubskaya, and N.N. Maksimov,** CABARET scheme for the numerical solution of aeroacoustics problems: generalization to linearized one-dimensional Euler equations, Comp. Mathematics Math. Phys., 2009, Vol. 49, No. 12, P 2168–2182.
7. **M.F. Ivanov, A.D. Kiverin, S.G. Pinevich, and I.S. Yakovenko,** Application of dissipation–free numerical method CABARET for solving gasdynamics of combustion and detonation, J. Phys.: Conference Series, 2016, Vol. 754, Iss. 10, P. 102003.
8. **V.Y. Glotov and V.M. Goloviznin,** CABARET scheme for two-dimensional incompressible fluid and in variables "stream function–vorticity", Math. Models and Computer Simulations, 2012, Vol. 4, No. 2. P. 144–154.
9. **M.C. Potter and E.J. Graber,** Stability of plane Poiseuille flow with heat transfer, Phys. Fluids, 1972, Vol. 15, No. 3, P. 387–391.
10. **D.P. Wall and S.K. Wilson,** The linear stability of channel flow of fluid with temperature-dependent viscosity, J. Fluid Mech., 1996, Vol. 323, P. 107–132.
11. **S.F. Urmancheev,** Flow of Thermoviscous Media, Herald of Nizhegorodkski University after N.I. Lobachevsky, 2011, Vol. 3, No. 4, P. 1197–1199.
12. **N. Taguelmimt, L. Danaila, and A. Hadjadj,** Effects of viscosity variations in temporal mixing layer, Flow, Turbulence and Combustion, 2016, Vol. 96, No. 1, P. 163–181.
13. **L. Voivenel, E. Varea, L. Danaila, B. Renou, and M. Cazalens,** Variable viscosity jets: entrainment and mixing process, Whither Turbulence and Big Data in the 21st Century? Ed. A. Pollard, L. Castillo, L. Danaila, M. Glauser. Springer International Publishing, 2017, P. 147–162.
14. **A.D. Nizamova, V.N. Kireev, and S.F. Urmancheev,** On stability of thermoviscous liquid flow, Herald of Tyumen State University. Physical and Mathematical Modeling. Petroleum, Gas, and Power, 2015, Vol. 1, No. 2, P. 104–111.
15. **Yu.M. Kulikov and E.E. Son,** Fluid flow with abrupt viscosity-temperature dependence, High Temperature, 2014, Vol. 52, No. 5, P. 723–729.
16. **Y.M. Kulikov and E.E. Son,** Stability of thermoviscous fluid flow under high temperature gradients, High Temperature, 2017, Vol. 55, No. 1, P. 131–138.
17. **Y.M. Kulikov and E.E. Son,** On stability of channel flow of thermoviscous fluid, Thermophysics and Aeromechanics, 2017, Vol. 24, No. 6, P. 883–900.
18. **Y.M. Kulikov and E.E. Son,** Kelvin–Helmholtz instability in thermoviscous free shear flow, J. Phys.: Conference Series, 2018, Vol. 946, P. 012075.
19. **I.H. Campbell and J.S. Turner,** The influence of viscosity on fountains in magma chambers, J. Petrology, 1986, Vol. 27, No. 1, P. 1–30.
20. **Yu.M. Kulikov and E.E. Son,** Taylor-Green vortex simulation using CABARET scheme in a weakly compressible formulation, European Phys. J. E, 2018, Vol. 41, P. 41.
21. **Y.M. Kulikov and E.E. Son,** The CABARET method for a weakly compressible fluid flows in one- and two-dimensional implementations, J. Physics: Conference Series. 2016, Vol. 774, P. 012094.
22. **P.E. Dimotakis,** The mixing transition in turbulent flows, J. Fluid Mech., 2000, Vol. 409, P. 69–98.
23. **M. Klein, A. Sadiki, and J. Janicka,** A digital filter based generation of inflow data for spatially developing direct numerical or large eddy simulations, J. Comput. Phys., 2003, Vol. 186, No. 2, P. 652–665.
24. **T. Lund, X. Wu, and D. Squires,** Generation of turbulent inflow data for spatially–developing boundary layer simulations, J. Comput. Phys., 1998, Vol. 140, No. 2, P. 233–258.

25. A.F. Kurbatskii and L.I. Kurbatskaya, Turbulent circulation above the surface heat source in a stably stratified environment, Thermophysics and Aeromechanics, 2016, Vol. 23, No. 5, P. 677–692.
26. M. Lesieur, Turbulence in Fluids. Springer Netherlands, 2008.
27. I. DeWolf, Divergence-free Noise. Martian Labs, 2018.
28. D. Schiavazzi, F. Coletti, G. Iaccarino, and J.K. Eaton, A matching pursuit approach to solenoidal filtering of three-dimensional velocity measurements, J. Comput. Phys., 2014, Vol. 263, P. 206–221.
29. C.M. de Silva, J. Philip, and I. Marusic, Minimization of divergence error in volumetric velocity measurements and implications for turbulence statistics, Exp. Fluids, 2013, Vol. 54, No. 7, P. 1557-1–1557-8.
30. C. Wang, Q. Gao, R. Wei, T. Li, and J. Wang, Weighted divergence correction scheme and its fast implementation, Exp. Fluids, 2017, Vol. 58, P. 44-1–44-14.
31. V.M. Goloviznin, M.A. Zaitsev, S.A. Karabasov, and I.N. Korotkin, New Algorithms for CFD Using Multiprocessor Computation Complexes, MSU Publ., Moscow, 2013.